energies

MDPI

Article

Enabling a Battery-Less Sensor Node Using Dedicated Radio Frequency Energy Harvesting for Complete Off-Grid Applications

Timothy Miller [1], Stephen S. Oyewobi [1], Adnan M. Abu-Mahfouz [1,2,*] and Gerhard P. Hancke [1]

[1] Department of Electrical, Electronic and Computer Engineering, University of Pretoria, Pretoria 0083, South Africa; u14060303@tuks.co.za (T.M.); oyewobistephen@gmail.com (S.S.O.); g.hancke@ieee.org (G.P.H.)

[2] Council for Scientific and Industrial Research (CSIR), Pretoria 0184, South Africa

* Correspondence: a.abumahfouz@ieee.org

Received: 4 August 2020; Accepted: 5 October 2020; Published: 16 October 2020

Abstract: The large-scale deployment of sensor nodes in difficult-to-reach locations makes powering of sensor nodes via batteries impractical. Besides, battery-powered WSNs require the periodic replacement of batteries. Wireless, battery-less sensor nodes represent a less maintenance-intensive, more environmentally friendly and compact alternative to battery powered sensor nodes. Moreover, such nodes are powered through wireless energy harvesting. In this research, we propose a novel battery-less wireless sensor node which is powered by a dedicated 4 W EIRP 920 MHz radio frequency (RF) energy device. The system is designed to provide complete off-grid Internet of Things (IoT) applications. To this end we have designed a power base station which derives its power from solar PV panels to radiate the RF energy used to power the sensor node. We use a PIC32MX220F32 microcontroller to implement a CC-CV battery charging algorithm to control the step-down DC-DC converter which charges lithium-ion batteries that power the RF transmitter and amplifier, respectively. A 12 element Yagi antenna was designed and optimized using the FEKO electromagnetic software. We design a step-up converter to step the voltage output from a single stage fully cross-coupled RF-DC converter circuit up to 3.3 V. Finally, we use the power requirements of the sensor node to size the storage capacity of the capacitor of the energy harvesting circuit. The results obtained from the experiments performed showed that enough RF energy was harvested over a distance of 15 m to allow the sensor node complete one sense-transmit operation for a duration of 156 min. The Yagi antenna achieved a gain of 12.62 dBi and a return loss of −14.11 dB at 920 MHz, while the battery was correctly charged according to the CC-CV algorithm through the control of the DC-DC converter.

Keywords: battery-less sensor nodes; RF harvesting; off-grid; wireless sensor networks; wireless power transfer

1. Introduction

In creating a smarter, more connected world, wireless sensor networks (WSNs) are becoming more widespread. The proliferation of the Internet of Things (IoT) has had a positive impact on a broad range of applications, including agriculture, medicine, and supply chain optimization [1]. The large scale and sometimes remote placement of sensor nodes makes the powering of such sensor nodes with wires or batteries impractical [2]. Improvements in communication technologies have made low power energy harvesting methods a viable solution of wireless power transfer to sensor nodes [3]. The increasing

popularity of the IoT has given rise to an increased demand for WSNs. WSNs allow for the placement of sensor nodes in difficult-to-reach remote locations. However, battery powered WSNs require the periodic replacement of batteries [4]. A less maintenance-intensive, more environmentally-friendly, compact alternative to battery powered sensor nodes are wireless, battery-less sensor nodes [5,6].

Such nodes are powered through wireless power transfer. Moreover, such sensor nodes will enable off-grid IoT applications such as smart lighting [7], surveillance of public spaces through battery-free video streaming [8,9], monitoring of environmental and habitat and alerting via battery-free cellphones [10], wildfire detection and prevention using smart camera networks, etc. [11]. Several power harvesting methods exist. A common method of power harvesting is the use of solar panels. This may not always be practical as the availability of energy is dependent in turn on the availability of solar illumination. Therefore, the focus of this work is the transmission of a dedicated RF signal and the subsequent harvesting of RF energy of the generated signal to provide wireless power transfer to a sensor node [12]. Radio frequency (RF) energy harvesting is a far-field, radiative wireless power transfer technique that can operate over distances ranging from several meters to kilometers [13–15].

Research has been conducted on the use of RF energy harvesting from both dedicated and non-dedicated sources. Non-dedicated sources incur no cost to the RF energy harvesting party, and do not affect the functioning of the RF source. Non-dedicated RF sources are comprised of RF transmitted by television transmitters, AM/FM radio transmitters, cellular base stations, Wi-Fi communication, etc. [16].

Dedicated RF sources have a multitude of frequency options, each with some constraint on the maximum allowable radiated power. However, exposure to RF energy can heat materials, including human body tissues, thus exposure to RF energy in excess can be unsafe. Therefore, rational safety standards needs to be adhered to while excessive safety margins that could compromise the effectiveness of systems need to be avoided [17]. Furthermore, dedicated RF sources are advantageous when a controllable energy supply is required. Narrowband antennas are suited to harvesting energy from dedicated RF sources. Due to the fact the RF power received is often low, the design of the antenna is an important contributing factor to the overall performance of the system [18]. The primary objectives for the antenna design are a high gain and high efficiency. Antennas can be either linearly or circularly polarized. Circular polarization may be advantageous for RF energy harvesting in that they minimize polarization mismatch losses [19]. However, an array of radiating elements may be set up to shape the radiation pattern as desired. Typically, an array of radiating elements is used to increase the gain. That is, to maximize the radiation in a particular direction, and minimize it in others [20]. Examples of the use of arrays of radiating elements is the antenna [21–24].

The RF received is converted to DC voltage by a rectification stage, which is often also used as a voltage multiplier. Various rectification topologies have been investigated with differing numbers of stages to produce the required voltage [25]. Fully cross-coupled rectifiers have good sensitivity and a high conversion efficiency.

In wireless battery-less sensor nodes deriving power from RF energy harvesting, the energy stored typically has a voltage that is not useable by microcontroller units or wireless communication modules. Typically, the energy stored has a voltage of less than 3.3 V, therefore, the voltage has to be boosted to a useable voltage. The challenges of harvesting RF energy become more pronounced as the distance over which energy is transferred increases. The power density of RF waves is inversely proportional to the square of the distance between the RF source and harvester. Furthermore, the Independent Communications Authority of South Africa (ICASA) does not allow more than 4 W effective isotropic radiated power (EIRP) to be radiated by RF sources at 920 MHz which limits the capability of harvesting energy from dedicated RF sources. Nonetheless, the proposed system can be deployed in a non-critical but difficult to reach areas, e.g., to take the temperature reading of a nuclear plant/high temperature furnace and send the readings to a human operator, who then acts on the reading to make a decision.

The problem addressed in this paper is how to develop a system that provides a sensor node with energy through RF energy harvesting. The main contributions of the paper are summarized as follows:

(1) We generate high voltage output from a low received RF power by designing an antenna with large gain and low return loss at 920 MHz.
(2) We design and implement specific aspects of the proposed system including the DC-DC converter, CV-CV charging algorithm, microcontroller unit, microcontroller firmware and the sensor node energy storage circuitry.
(3) We design and implement a proportional integral derivative (PID) to control the DC-DC converter to ensure a stable output current and voltage of the step-down DC-DC converter.
(4) We develop a constant current-constant voltage (CC-CV battery) charging algorithm to effectively charge lithium-ion batteries to prevent permanent damage due to overvoltage or overcurrent conditions.
(5) We develop an energy harvesting system that provides 140 mW of power for a duration of 2.14 s once every 156 min.

The rest of the paper is structured as follows: Section 2 presents the related work. Section 3 describes the theory of the design, whereas the design alternatives and implementation is presented in Section 4. Our findings is presented and discussed in Section 5. A summary of results achieved is presented in Section 6. Section 7 concludes the paper.

2. Related Works

Several power harvesting methods exist. In [26], its authors examined the various architectures, energy sources, and storage technologies in energy harvesting sensor systems. In [27] the authors proposed an RF energy harvesting supply that is very efficient and highly sensitive. The objective of the designed harvester which comprises a single-series circuit with one double diode is to provide the least reflection coefficient and a high rectification efficiency. This was achieved by considering the rectifier micro strip trace dimensions and load as well as the impedance matching network. In another related work, in [28] the authors designed an electrically small as well as efficient and sensitive rectenna for harvesting ultra-low power RF energy. They exploited rectenna-array configuration to increase the DC output voltage in order to deliver low power density levels to the load. A common method of power harvesting is the deployment of solar panels. In [29], an approach of harvesting solar radiant energy by the use of a nanofluid concentrating parabolic solar collector was proposed. However, this method may not be efficient as the availability of energy depends on the availability of solar illumination. RF energy harvesting is a solution that eliminates the energy dependency on solar illumination. In [30], an RF energy harvesting system operating from 865.7 to 867.7 MHz using resonant inductive coupling radio frequency identification (RFID) technology was proposed. The limitation of this technique is the large loss of power over distances longer than a few meters. However, RF energy harvesting using the radiative wireless power transfer technique can operate over long distances. In [31], the authors investigated if wireless energy transfer is possible through the living body. As a result, they examined energy harvesting through of RF, heat and vibration. Afterwards, they presented system architecture and circuitry of effective energy transfer and harvesting techniques. Similarly, the work in [32] provides justification for energy harvesting from external ambient sources. Furthermore, they proposed RF energy harvesting technique in the 935–960 MHz frequency range. This objective was achieved by receiving more power from the antenna through impedance matching. Additionally, incoming RF signal is converted to DC signal through a rectifier circuit and boosted by a chopper circuit before it is fed to the battery. In [33], its authors showed by means of a sampling theorem using a statistical model that the amount of energy harvested is linearly related to amount of incident energy. Then, they used their findings to develop the statistical characteristics of harvested energy in a series of N harvesting blocks. In another work [34] multiple dedicated RF sources was proposed for an efficient RF energy harvesting system to avert energy holes. The optimum energy transmission challenge was solved as an optimization problem with minimum energy charge by each node as the constraints. Some of the shortcomings of the proposed techniques are that the sensor nodes

are constantly on while receiving the RF energy, and the received RF energy needs to be greater than the energy required by sensor nodes to operate. Therefore, the main contributions of our proposed system is to mitigate the abovementioned shortcoming.

3. Theory

The schematic diagram of the setup functional analysis is shown in Figure 1. The power base station (FU1) is powered via radiant solar energy. Radiant energy is converted to electrical energy by the solar panel (FU1.1). This electrical energy is conditioned by the direct current-direct current (DC-DC) converter as well as the CC-CV charging circuit (FU1.3) and stored in the battery (FU1.4). Stored electrical energy is used to power the RF transmitter (FU1.5), and RF transmitter amplifier (FU1.6). The transmitting antenna (FU1.7) transmits the amplified RF signal. The sensor node (FU2) is powered via RF energy. The rectenna (FU2.1) of the sensor node (FU2) receives the transmitted RF signal and rectifies the signal. The rectified signal is harvested by the RF harvesting circuit (FU2.2) and is stored by the energy storage component (FU2.3) which is a capacitor. Energy is accumulated over a period of time and is subsequently used to power the temperature sensor and the long range (LoRa) transceiver (FU2.5) [35]. The user base station (FU3) consists of a LoRa transceiver (FU3.1) and a liquid crystal display (LCD) screen (FU3.2) and derives its power from the grid. The user base station LoRa transceiver (FU3.1) receives data from the sensor node LoRa transceiver (FU2.5). The data is displayed on a graphical user interface (FU3.2) in the form of an LCD screen. In Table 1, the technical deliverables of the system are shown.

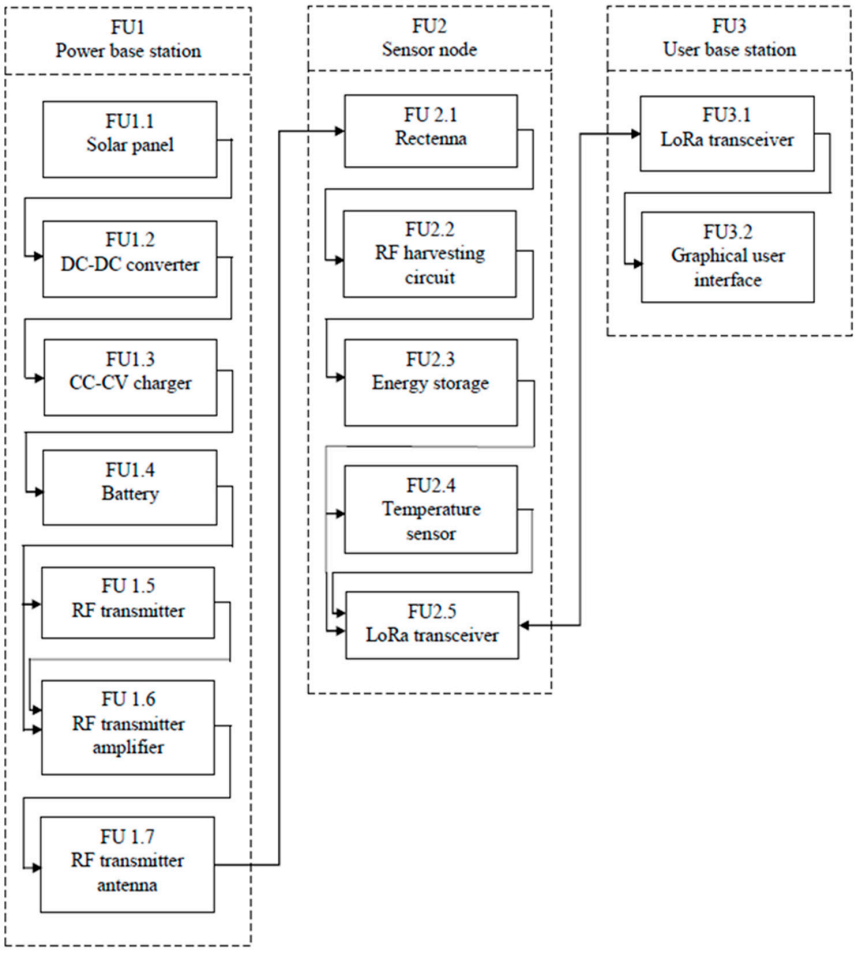

Figure 1. A schematic diagram of the setup.

Table 1. Technical deliverables of the system.

Deliverables	Designed and Implemented	Off-the-Shelf	Location of Each Deliverables
Solar panel		✓	FU1.1
Battery		✓	FU1.4
DC-DC converter	✓		FU1.2
CC-CV charging circuit	✓		FU1.3
RF transmitter		✓	FU1.5
RF transmitter amplifier		✓	FU1.6
RF transmitter antenna		✓	FU1.7
Temperature sensor		✓	FU2.4
LCD screen		✓	FU3.2
LoRa transceiver		✓	FU2.5/FU3.1
Microcontroller unit		✓	FU1.2/FU1.3
Microcontroller firmware	✓		FU1.2/FU1.3
Rectenna	✓		FU2.1
RF harvesting circuit	✓		FU2.2
Sensor node energy storage circuitry	✓		FU2.3

4. Design Alternatives and Design Implementation

The sequence of the design follows the path of energy transfer from the solar panel to the batteries to the RF amplifier to the receiving antenna and to the energy harvesting circuit. A complete system visualization is shown in Figure 2.

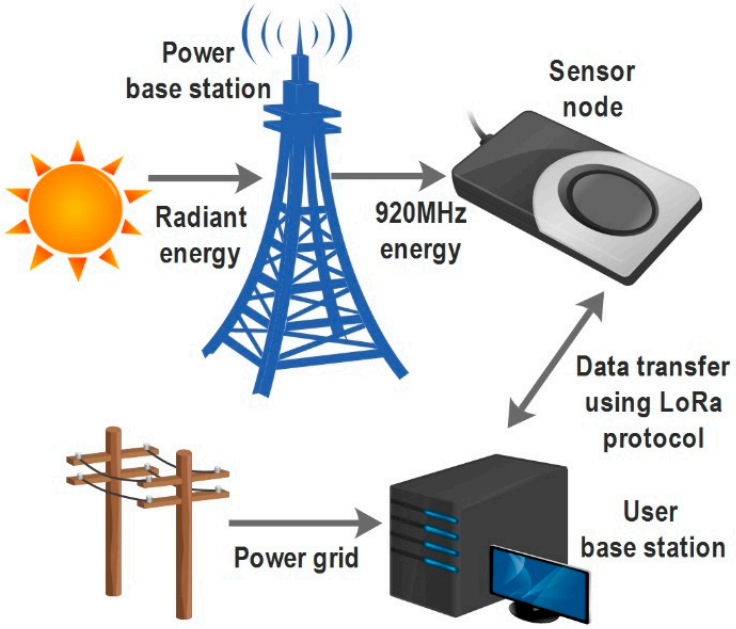

Figure 2. System visualization.

4.1. Power Base Station (FU1)

The reason for implementing a power base station is to use the harvested solar energy to charge lithium-ion batteries which in turn are used to power the RF transmitter. Firstly, the voltage from the solar panel needs to be stepped down to a desired voltage level. To achieve this, either a linear regular or a DC-DC converter can be utilized. In this work a DC-DC converter was selected because of its higher efficiency in stepping down voltage. Similarly, the CC-CV charging algorithm used for effectively charging the batteries can either be executed by a current limiting circuit cascaded with a voltage limiting circuit or by controlling the DC-DC converter with a microcontroller. Furthermore, a MOSFET

instead of an IGBT was used as a switch for the DC-DC converter due to a MOSFET medium output impedance and fast switching speed. This is because an increase in switching frequency will result in a decrease output current and voltage ripple [36–38].

4.2. Step-Down DC-DC Converter Design (FU1.2)

The purpose of the DC-DC converter is to step the voltage fed by the 50 W solar panel down to the voltage required to charge Li-ion batteries. The converter is controlled using a high frequency pulse width modulated (PWM) signal generated by a microcontroller. The duty ratio of the PWM signal determines the output voltage of the converter. The power base station requires two 2200 mAh Li-ion batteries to operate. It was decided to place the batteries in series. This decision was made to ensure that at any state of charge, the batteries combined voltage would be greater than 5 V. Additionally, the batteries being placed in series requires less current to flow through the step-down DC-DC converter than if they were placed in parallel. A higher output voltage requires a higher duty ratio which results in a slightly higher overall efficiency. A switching frequency of 50 kHz was determined through practical observation to provide acceptable output ripple and small enough losses. To fulfil the requirements of the CC-CV charging of the Li-ion batteries connected in series, the converter should have an output current I_0 of 1.1 A and an output voltage V_0 ranging from 5.6 V to 8.4 V (2.8 V to 4.2 V per cell). Ferrite toroidal inductors were selected due to low magnetic losses. The resistance of one inductor was measured as R_L = 375 mΩ. In practical implementation of the converter, four inductors were placed in series yielding a total resistance of R_L = 1.5 Ω. The inductance of each inductor was chosen to be 88 mH for a total inductance of L = 352 mH. An electrolytic capacitor with a capacitance of C = 3300 was chosen. From the PR6003-T diode datasheet, the forward voltage drop is given as V_{fwd} = 1.2 V. Whereas, in the IRF3205 datasheet, the drain-to-source current is given as $I_D = 1.1A$. In the CSRB20G10L00 datasheets, shunt resistor is given as R_{sh} = 10 mΩ. Due to the resistance of the inductors being significantly higher, the shunt resistance was taken to be negligibly small, thus R_{sh} = 0 mΩ. Two cases were considered in the theoretical analysis DC-DC converter to determine the minimum size of the storage components.

Case 1: when $V_o = 8.4$V and $I_O = 1.1$A

$$I_{L,avg} = I_{O,avg} \tag{1}$$

$$\delta = \frac{V_o + I_{o,avg}R_L + V_{fwd}}{V_{in} - V_{DS} + V_{fwd}} = 0.5859 \tag{2}$$

The voltage across the inductor is taken by applying the Kirchhoff voltage law to the converter when the MOSFET is on:

$$V_L = V_{in} - I_{L.avg}R_L - V_{DS} - V_o = 7.95 \text{ V} \tag{3}$$

To ensure that the converter operates in continuous conduction mode, the current ripple ($\Delta i_{L,pk-pk}$) should not exceed a maximum value of $\Delta i_{L,pk-pk} = 2.2$ A with a switching frequency of $f_{sw} = 50$ kHz the minimum size of the inductor was calculated as:

$$L = \frac{V_L \times \delta \times T_{sw}}{\Delta i_{L,pk-pk}} = 42.3446 \text{ μH} \tag{4}$$

With an output current ripple of $\Delta i_{L,pk-pk} = 2.2$ A, to maintain a maximum output voltage ripple of $V_{o,pk-pk} = 10$ mV, the minimum size of the capacitor was calculated as:

$$V_{C,pk-pk} = V_{O,pk-pk} \tag{5}$$

$$C = \frac{\Delta i_{L,pk-pk}T_{sw}}{8 \times \mathrm{V}_{C,pk-pk}} = 550 \text{ μF} \tag{6}$$

The average input current $I_{in,avg}$ was calculated as:

$$I_{in,avg} = \delta \times I_{O,avg} \ = \ 0.6445 \text{ A} \tag{7}$$

The input power (P_{in}) was calculated as:

$$P_{in} = V_{in} \times I_{in,avg} = \ 11.601 \text{ W} \tag{8}$$

The output power (P_o) was calculated as:

$$P_o = V_o \times I_{o,avg} \ = \ 9.240 \text{ W} \tag{9}$$

The overall efficiency (η) was calculated as:

$$\eta = \frac{P_o}{P_{in}} \times 100 \ = \ 79.65\% \tag{10}$$

Case 2: when $V_o = 5.6$ V and $I_O = 1.1$ A, and by applying Equation (2) $\delta = 04401$. The voltage across the inductor is obtained using Equation (3) as $V_L = 7.950$ V. Also, with the maximum current ripple of $\Delta i_{L,pk-pk} = 2.2$A and a switching frequency of $f_{sw} = 50$ kHz the minimum size of the inductor was obtained using Equation (4) as $L = 31.181$ µH. Furthermore, with the maximum current ripple of $\Delta i_{L,pk-pk} = 2.2$ A, to maintain a maximum output ripple of $V_{O,pk-pk} = 10$ mV, the minimum size of the capacitor was obtained using Equations (5) and (6) as $C = 550$ µF. Whereas, the average input current $I_{in,avg}$ was obtained as 0.4841 A using Equation (7) the input power (P_{in}) was obtained as 8.7140 W using Equation (8) and the output power (P_o) using Equation (9) is obtained as 6.1600 W. Therefore, the overall efficiency (η) was calculated as:

$$\eta = \frac{P_o}{P_{in}} \times 100 \ = \ 70.69\% \tag{11}$$

4.3. Microcontroller Input Design

Due to the solar PV input to the DC-DC converter, and the CC-CV Li-ion battery charging output of the DC-DC converter, both the input and output of the converter are variable. As such there exists the need for a dynamic control of the converter according to its input and output. By extension, there is a need for circuitry that acts as input to the microcontroller. To monitor the voltage output, a simple voltage dividing network of resistors was used in conjunction with a non-inverting operational amplifier. The circuit that provides voltage information to the microcontroller was simulated using OrCAD and is shown in Figure 3.

With an input voltage of $V_{in} = 2.1$ V and a resistance $R_f = 12$ kΩ and $R_{in} = 560$ kΩ the output of the non-inverting amplifier was calculated as:

$$V_{out} = \frac{R_f}{R_{in}} \times V_{in} \ = \ 2.145 \text{ V} \tag{12}$$

The calculated output voltage value is congruent with the simulated output voltage value. To monitor the current output, the voltage across a 10 mΩ shunt resistor was fed through a differential operational amplifier. However, due to the large voltage outputs from the difference amplifier when no current flows through the shunt resistor, the output of the difference amplifier was fed to a non-inverting amplifier with a supply voltage of 3.3 V. This is to ensure that the voltage present on the ADC input pin of the microcontroller does not exceed 3.3 V. The circuit that provides current information to the microcontroller is shown in Figure 4.

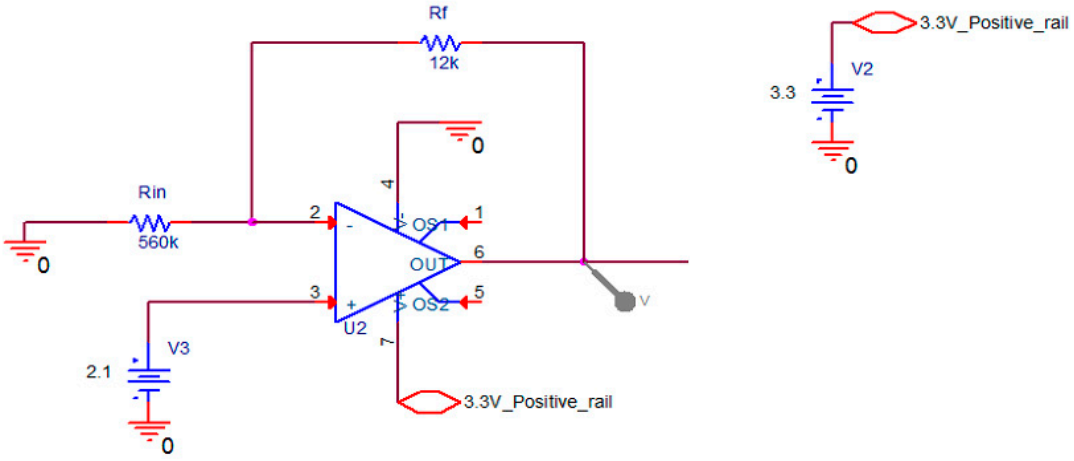

Figure 3. Voltage information scaling circuit.

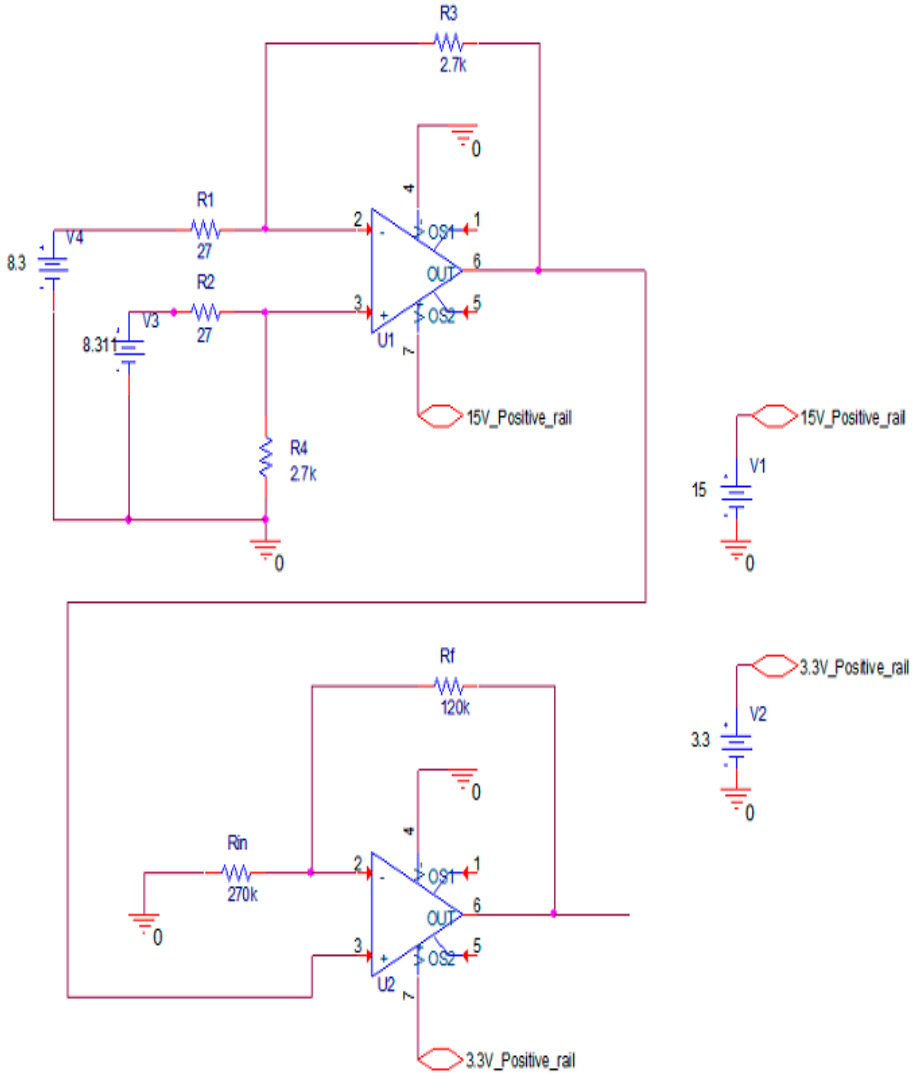

Figure 4. Current information scaling circuit.

The expected input to the differential amplifier is the voltage across the 10 mΩ shunt resistor. Assuming a current of 1.1 A flows through the shunt resistor the voltage difference will be 11 mV.

When the resistors are selected such that $R1 = R2$ and $R3 = R4$ the differential amplifier equation is simplified to:

$$V_{out,\,difference} = \frac{R3}{R1}(V3 - V4) \tag{13}$$

With $R3 = 2.7$ kΩ, $R1 = 27$ Ω and $V3 - V4 = 11$ mV we obtained $V_{out,\,difference} = 1.1$ V. The output of the non-inverting amplifier was obtained as:

$$V_{out,\,non-inverting} = \frac{Rf}{Rin} V_{out,difference} = 1.5889\ \text{V} \tag{14}$$

The simulated output values of $V_{out,\,difference} = 1.1$ V and $V_{out,\,non-inverting} = 1.6029$ V are congruent with the calculated values.

4.4. Microcontroller Firmware Design

The microcontroller chosen for the control of the DC-DC converter and implementation of the CC-CV charging of the Li-ion batteries was the PIC32MX220F032 (Microchip, Chandler, AZ, USA). To meet the requirements of the CC-CV battery charging system, the microprocessor needs to meet a number of requirements. The resolution of the analogue to digital display (ADC) module affects how accurately the microprocessor reads the voltage and current outputs of the DC-DC converter. The resolution of the PWM module affects how accurately the microprocessor adjusts the duty ratio of the MOSFET in the DC-DC converter. The instruction clock frequency affects how rapidly the control system implemented on the microprocessor responds to differences between the desired set-point and the actual output. The requirements of the microprocessor are summarized in the Table 2.

Table 2. Summary of processor features.

Feature	Required	PIC32MX220F032
ADC inputs	3	9
ADC resolutions	10 bits	10 bits
PWM outputs	1	16
PWM resolutions	10 bits	10 bits with an instruction clock frequency of 40 MHz and a PWM frequency of 50 kHz
Instruction clock frequency	1 MHz	Up to 40 MHz

In Figure 5, the program flow of the implementation of the microcontroller firmware is presented.

4.5. PID Controller Design

To ensure a stable output current and voltage of the step-down DC-DC converter, a proportional integral derivative (PID) control was applied to the converter. This is of importance when dealing with lithium-ion rechargeable batteries which can experience permanent damage if exposed to overvoltage or overcurrent conditions. Therefore, a continuous cycling test was performed to obtain the ultimate period (P_u) and the ultimate gain (K_u) of the system responsible for controlling the CC-CV charging of the Li-ion batteries. Based on the experiment performed, the ultimate gain associated with the undamped response of the system was recorded as $K_u = 0.1525$ µs whereas the ultimate period of the undamped response was measured as $P_u = 520$ µs. Subsequently, the obtained ultimate gain and ultimate period of the system were used to calculate the tuning parameter of the PID. In addition, the continuous cycling method used to obtain the ultimate gain and ultimate period is often used in conjunction with the Ziegler-Nichols tuning parameters. However, because the Ziegler-Nichols tuning parameters is undesirable for the CC-CV charging algorithm a less aggressive Tyreus-Luyben modified Ziegler-Nichols tuning rules were applied. The Ziegler-Nichols tuning parameters has a decay ratio which produces a response with overshoot and short settling time which often result in over-voltage or over-current. The Tyreus-Luyben tuning parameters are given in Table 3.

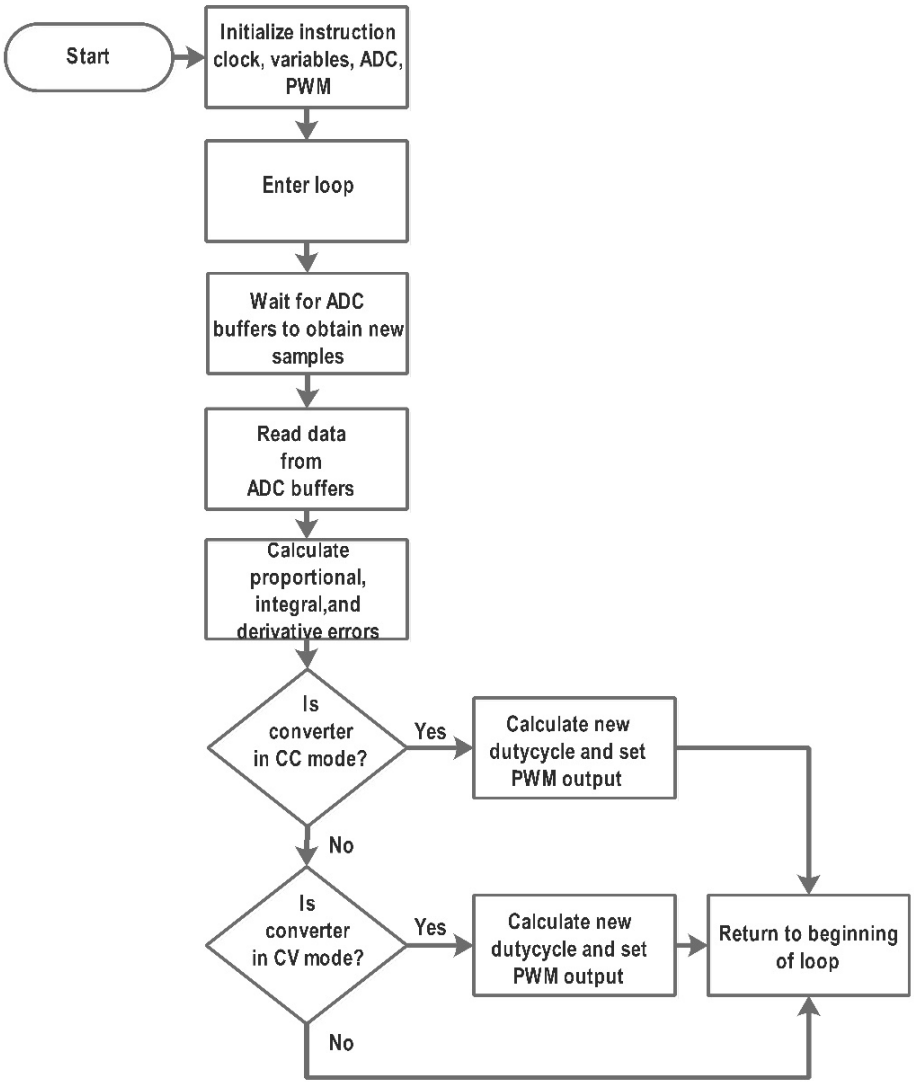

Figure 5. Flowchart of the implementation of the microcontroller firmware.

Table 3. Tyreus-Luyben tuning parameters.

	K_c	τ_I	τ_D
PID controller	0.313 K_u	2.2 P_u	$\frac{P_u}{6.3}$

Based on the experimentally obtained ultimate gain and ultimate period, the Tyreus-Luyben tuning parameters were calculated as follows: $K_c = 0.313\ K_u = 0.04773$, $\tau_I = 2.2 P_u = 0.01144$ and $\tau_D = \frac{P_u}{6.3} = 0.00008254$. Thereafter, the PID control is implemented through the PIC32MX220F032 microcontroller.

4.6. Antenna (FU2.2)

A stacked micro-strip patch antenna was selected to be used as the antenna type. The antenna was simulated using FEKO with various materials. After several iterations of design, a 0.7 mm thick copper conductor was selected and polystyrene was selected for the substrate. However, the stacked micro-strip patch antenna did not meet the requirements of the system. Therefore, the approach was adjusted and a Yagi antenna [39], which consists of the stacking of $\mp 1/2$ dipoles was designed. The antenna implementation flow diagram is shown in Figure 6.

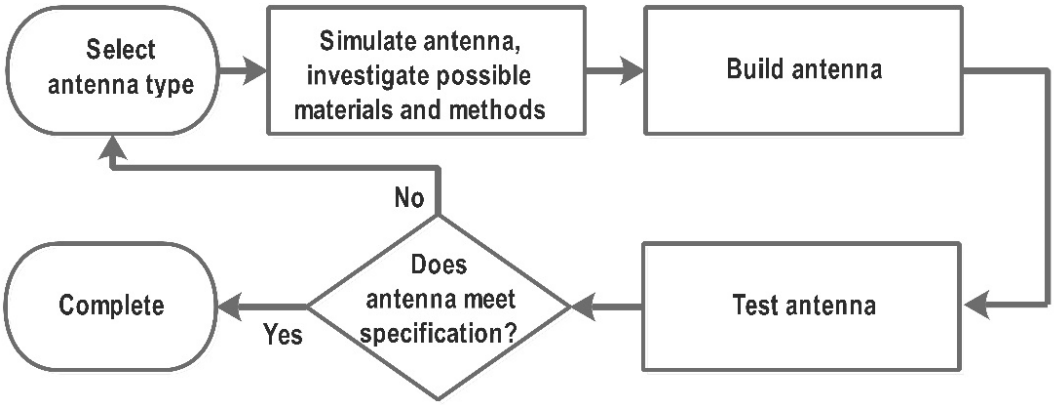

Figure 6. Antenna implementation flow diagram.

4.7. Yagi Antenna Design

The starting point for the Yagi antenna design was obtained from the National Bureau of Standards (NBS) paper [40] with adjustment of the reflector spacing to 0.25 lambda which has been found to be a near optimum value [41]. The thickness, length and spacing of the antenna elements affect the overall performance of the antenna. It was decided to set a fixed element thickness based on availability of materials. Using this element thickness, the element spacing and lengths were optimized. It was found that aluminum rods were available with an outer diameter of 6.35 mm and copper rods were available with an outer diameter of 6 mm. The active element (folded dipole) was to be constructed with copper rod, and the parasitic elements (reflector and directors) were to be constructed with aluminum rod. The Yagi antenna was simulated using the FEKO electromagnetic simulation software. The Yagi antenna was simulated with perfect electrical conductors (PEC) as the resistance present on aluminum and copper rods is sufficiently small to be considered zero. The antenna was simulated without the conducting aluminum tube boom. This was found to be computationally expensive and impractical for optimization searches. As such, the antenna was optimized using free-standing elements. A boom correction factor obtained from experimental data was applied to the elements before construction of the antenna. An optimization search was set up to optimize the realized gain and return loss at 920 MHz. It was found that optimizing for total gain as opposed to realized gain would compromise the return loss goal. The length and spacing of the director, reflector and driven elements were entered as parameters in the optimization search. The final iteration of the Yagi antenna optimization had a simulated gain of 15.0108 dBi and a return loss of −21.7774 dB at 920 MHz. The Yagi antenna dimensions are summarized in Table 4. The driven element length is given from tip to tip which is more significant than the total length of the folded rod.

Table 4. Yagi antenna dimensions.

Element	Spacing from the Driven Element (mm)	Length (mm)	Diameter (mm)
Reflector	64.5	169.55	6.35
Driven	0	184.1	6.00
Director 1	26.2	150.3	6.35
Director 2	86.6	149.4	6.35
Director 3	157.6	146.1	6.35
Director 4	239.4	145.7	6.35
Director 5	333.6	144.4	6.35
Director 6	434.2	139.8	6.35
Director 7	538.7	141.4	6.35
Director 8	647.9	140.8	6.35
Director 9	760.2	140.0	6.35
Director 10	879.5	137.6	6.35

A table saw was used to cut the aluminum tube and rod into the desired sizes. Pieces of wood were cut and measured to obtain the desired length before cutting the aluminum. The director and reflector elements were filed and measured with a Vernier gauge to obtain an accuracy of within 0.2 mm. A drill press was used to drill holes into the Aluminum tube and the director and reflector elements were tapped into their respective holes. The copper rod was cut using a hack saw and was bent using a wooden jig. The folded dipole was attached to the aluminum tube using metal corner pieces, hose clamps, and a nut and bolt. Figure 7 shows the designed Yagi antenna.

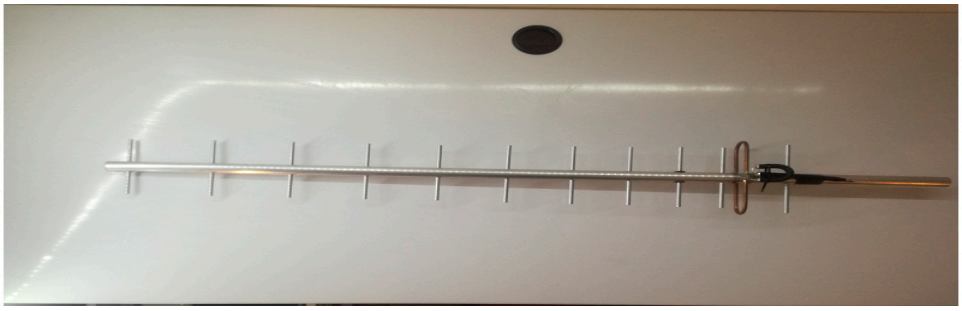

Figure 7. Implemented Yagi antenna.

4.8. Energy Harvesting Circuit (FU2.2)

The intended achieved gain for the antenna was 6 dBi. Assuming that this was achieved, an input power of −11.44 dBm would be available when the sensor node is placed 15 m from the RF source. This input power does not require a highly sensitive RF-to-DC converter. As such, the diode-based Dickson RF-DC converter (city, state abbrev if USA, country) was chosen. The Dickson RF-DC rectifier was simulated using the HSMS-2860 Schottky diode model and ideal capacitors. When tested, the Dickson RF-DC converter did not have a high enough efficiency. The approach was adjusted, and a transistor based fully cross-coupled rectifier circuit was designed. The fully cross-coupled rectifier circuit was simulated using HFA3096 transistors (Renesas, city, state abbrev if USA, country_ and ideal capacitors. Simulations of the energy harvesting circuit were done in LTSpice XVII, a high performance SPICE simulation software. LTSpice XVII has circuit capture and waveform viewer functionality. The RF-DC flow diagram is shown in Figure 8.

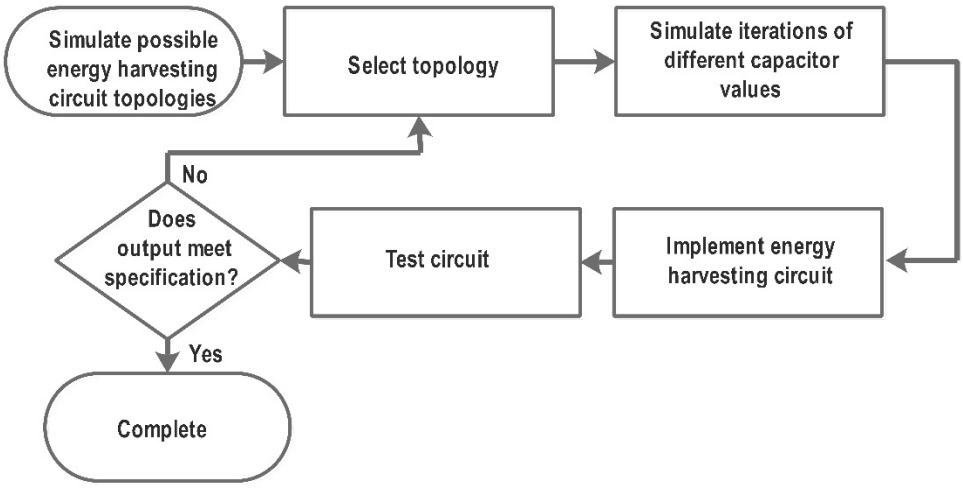

Figure 8. RF-DC converter flow diagram.

4.9. Energy Harvesting Circuit Design (FU2.2)

4.9.1. Fully Cross-Coupled RF-DC Converter

A transistor-based fully cross-coupled radio frequency-direct current (RF-DC) converter circuit was simulated using LTSpice XVII. Additionally, a Renesas HFA3096BZ ultra high frequency transistor arrays were selected for the fully cross coupled RF-DC converter. Furthermore, the fully cross-coupled RF-DC converter was simulated with one and two stages. However, it was found that the 2-stage circuit was approximately half as efficient and did not provide a significant increase in voltage across the storage capacitor. Therefore, a single stage fully cross-coupled RF-DC converter circuit with Renesas HFA3096BZ transistor is implemented. The implemented circuit is presented in Figure 9.

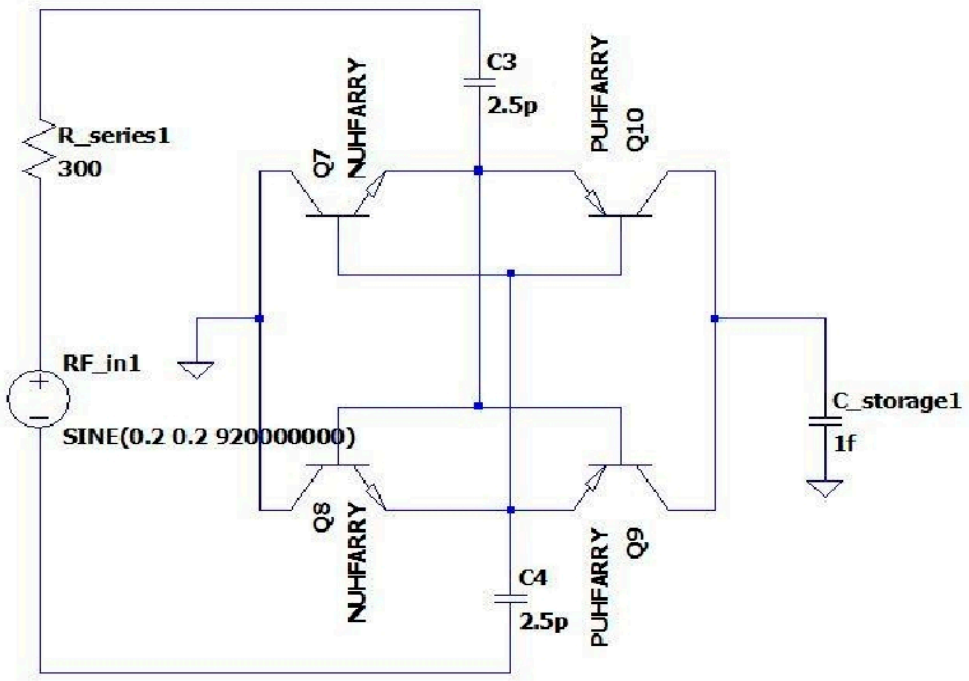

Figure 9. Single stage fully cross-coupled RF-DC converter circuit with Renesas HFA3096BZ transistor.

4.9.2. Step-Up DC-DC Converter

The boost converter was designed to be controlled by a microcontroller. In order to provide the microcontroller with the necessary voltage, a 551 timer is turned on through the use of a momentary switch. The 551 timer drives the boost converter MOSFET while the momentary switch is on. The boost converter outputs a voltage which is regulated to 3.3 V and fed to the microcontroller. Once the momentary switch is released (off), the MOSFET is driven by the microcontroller. The purpose of the DC-DC converter is to boost the voltage stored on the supercapacitor to a voltage usable by the sensor node (≥3.3 V). The step-up converter was designed to be connected to a 3.3 V low dropout voltage regulator. The converter is controlled using a high frequency PWM signal generated by a microcontroller. The duty ratio of the PWM signal determines the output voltage of the converter. The frequency of the PWM signal has an inverse relationship on the output current and voltage ripple; An increase in the switching frequency results in a decrease in ripple. The frequency is directly proportional to switching losses of the MOSFET, and hysteresis losses of the inductor. The voltage regulator was assumed to have a 250 mV dropout while delivering the required current. The MOSFET is assumed to have a drain-source voltage drop of $V_{DS} = 42$ mV. The diode is assumed to have a forward voltage drop of $V_{fwd} = 320$ mV. The resistance of the inductor is assumed to be $RL = 250$ mΩ. The boost converter was simulated with a switching frequency of $f_{sw} = 1$ kHz. The step-up DC-DC converter was simulated using LTSpiceXVII. The simulation was used to evaluate 16 different MOSFET

options, and nine different diode options. Once the most suitable MOSFET and diode options were chosen, the circuit was simulated using ideal voltage controlled switches to charge a capacitor representing a supercapacitor, and to subsequently provide the converter with an input voltage from the supercapacitor. The MOSFET was controlled using a 3.3 V PWM voltage source. A constant power load was powered by the boost converter through a 3.3 V voltage regulator. The power consumption of the load was calculated using the expected power draw of the sensor node as well as the efficiency of the voltage regulator which lies between the step-up converter and the MDOT module. The duty cycle of the PWM voltage source, inductance and capacitance were adjusted to optimize the time that the load could be supplied with a voltage greater than 3 V. Using the selected components, the step-up converter was simulated to determine the optimum size of the capacitor. The boost converter was simulated using the maximum effective constant duty cycle to determine the minimum size supercapacitor required to provide 140.0 mW of power for a duration of 2.14 s. It was found that the optimum output capacitance was 200 µF and that the minimum capacitance of the supercapacitor was 2 *F*. Figure 10 shows the sensor node circuit containing the fully cross-coupled RF-DC converter, the step-up DC-DC converter, the MDOT LoRa module [42,43], and the Microchip MCP9700 temperature sensor.

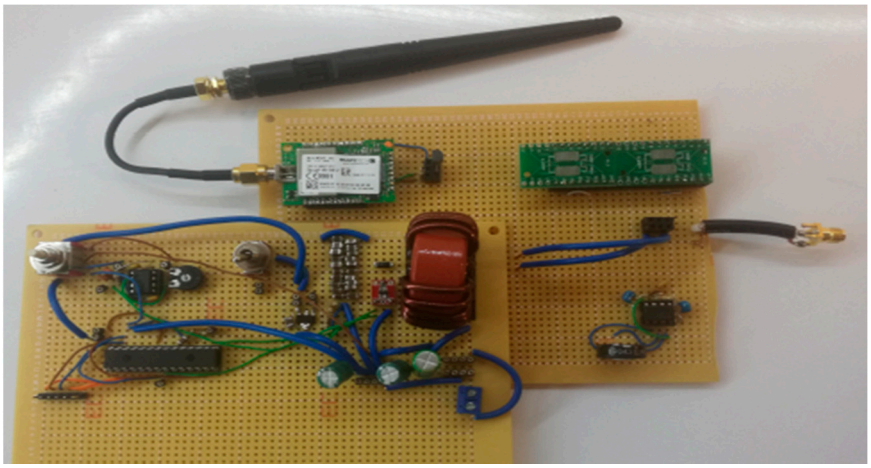

Figure 10. Sensor node circuit with other implemented circuits.

4.10. Design of the Multitech LoRa Communication

To implement LoRa communication, two LoRa MDOT-868 modules (Multitech, Mounds View, MN 55112, USA) were used. The Multitech MTUDK2-ST-MDOT development board was used to program the LoRa modules. The arm mbed development platform's compiler was used to alter and compile code. The MDOTs work in peer-to-peer mode using example code from Multitech. In peer-to-peer mode, the MDOTs are constantly in receive mode, unless transmitting data.

4.11. Sensor Node

Apart from the transmission of data to the user, the main objective in the design of the sensor node MDOT firmware was to transmit data in the shortest timeframe possible and thus decrease the overall energy requirement of the sensor node. The join delay was set to 1 ms. The default join delay is 5 s. The transmit power was set to the lowest level of 2 dBm. The data rate was set to the fastest available data rate for use in the Europe region. Although the higher data rate consumes more power, the MDOT operates for a shorter duration which improves overall energy consumption. Two possible temperature sensor ICs were investigated. Table 5 shows a comparison of the features of the Dallas 18B20 and Microchip MCP9700 temperature sensors.

Table 5. Temperature sensor comparison.

Temperature Sensor	Dallas 18B20	Microchip MCP9700
Operating Voltage	3.0 to 5.0 V	2.3 to 5.5 V
Accuracy	± 0.5 °C	± 0.4 °C
Standby Current	900 ηA	6 μA
Active Current	1 mA	6 μA
Temperature Conversion Time	750 mA	N/A

The Microchip MCP9700 was selected for use in the sensor node due to its low active current and lack of conversion time. The sensor node MTDOT obtains a temperature reading from the Microchip MCP9700 temperature sensor via the mbed AnalogIn Driver Application Programming Interface (API). The temperature float variable is split into two integers, one representing the whole number and the other representing the fraction. The two integers are concatenated into one longer integer and sent via LoRa to the user base station MDOT. For debugging purposes during the development of the MDOT firmware, the temperature value read from the temperature sensor was outputted to the serial port.

5. Results and Discussion

The section presents result of qualification tests performed to validate the performance of the proposed system.

5.1. Full System Test

The main objectives of this test were to test the system as a whole and to determine over what period of time the sensor node can harvest enough energy to obtain and send data to the user base station. The following procedure was used to conduct the test: (1) The storage capacitors of the sensor node were discharged using a 2.7 Ω resistor, (2) The frequency synthesizer was set to output a 920 MHz continuous wave (CW) signal at an output power of 2 dBm, (3) The sensor node was placed within line-of-sight 15 m from the power base station, (4) The direction and polarity of the sensor node antenna were adjusted to be in the direction and polarity of the RF source, (5) The frequency synthesizer was set to output a 920 MHz CW signal at an output power of 2 dBm, (6) The RF amplifier was turned on and the timer was started, (7) The voltage across the terminals of the storage capacitor were measured at 10-min intervals, (8) Once the voltage reached 1 V, the step-up DC-DC converter was switched on using a mechanical switch powering the MDOT LoRa module and MCP9700 temperature sensor, (9) The voltage across the storage was recorded after the voltage collapse of the step-up converter. Figure 11 shows the voltage profile over period of 360 min.

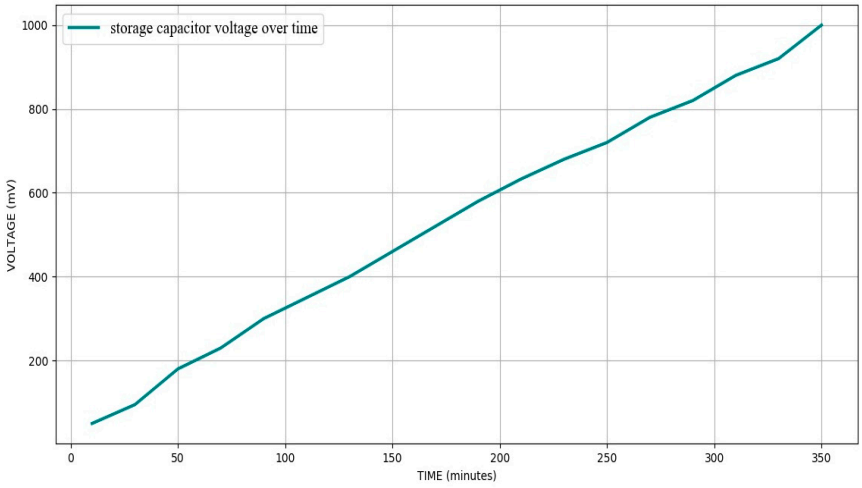

Figure 11. Storage capacitor voltage overtime.

The step-up converter was switched on with an input voltage of 1 V. The voltage stored on the storage capacitors after the step-up converter experienced output voltage collapse was 600 mV. The test confirms that the system is able to operate with a 15 m distance between the sensor node and RF source. The test shows that the sensor node is able to harvest enough energy to obtain and transmit data over a period of 156 min. The sensor node sent data to the user base station successfully. The data was displayed on the user base station LCD display.

5.2. Yagi Antenna Gain Test

The main objective of this test was to measure the gain relative to a lossless isotropic antenna (dBi) performance of the implemented Yagi antenna. The following procedure was used to conduct the test: (1) The antenna was mounted on the aluminium rod, (2) The antenna was connected to the testing apparatus via an SMA cable, (3) The frequency range over which the gain would be measured was set, (4) The direction of the main lobe of the antenna was adjusted to direct the maximum gain at 0.92 GHz towards the center of the reflector, (5) A frequency sweep was performed, (6) The Yagi antenna was removed and a reference horn antenna was connected, (7) The direction of the main lobe of the horn antenna was adjusted to direct the maximum gain a 0.92 GHz towards the center of the reflector, (8) A frequency sweep was performed, and (9). The results were obtained by comparing the Yagi antenna and reference antenna measurements using MATLAB. The results were stored in a text file. Figure 12 shows the measured gain (dBi) versus frequency (GHz) of the Yagi antenna.

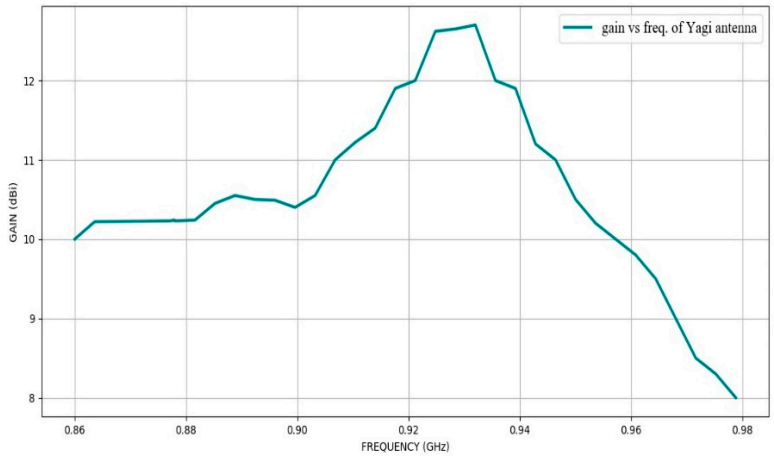

Figure 12. The measurement gain (dBi) versus frequency (GHz) of the Yagi antenna.

The gain of the antenna at the desired frequency was measured as 12.62 dBi. This complies with the proposed specification of at least 1 dBi. The test was a success.

5.3. Yagi Antenna Return Loss Test

The main objective of this test was to measure the return loss (dB), and the Voltage Standing Wave Ratio (VSWR, unitless) performance parameters of the implemented Yagi antenna. The following procedure was used to conduct the test: (1) The antenna was placed on a wooden stool, (2) The antenna was connected to the testing apparatus via an SMA cable, (3) The frequency range over which the gain would be measured was set, (4) The spectrum analyzer test was performed, (5) The results were recorded in a text file. Figures 13 and 14 show the return loss versus the frequency and the VSWR versus frequency respectively.

The return loss and VSWR measurements show that the antenna has the highest efficiency from 0.92 GHz to 0.9332 GHz. At 0.92 GHz the return loss was measured as −14.11 dB and the VSWR was measured as 1.4906.

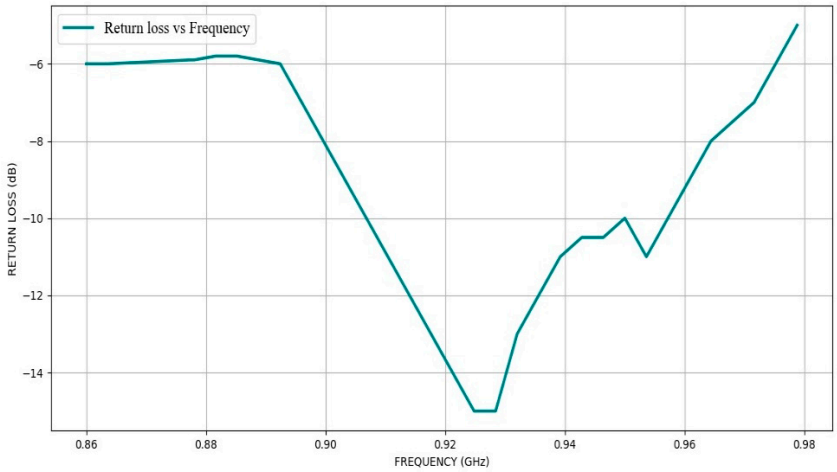

Figure 13. The return loss (dB) versus frequency (GHz).

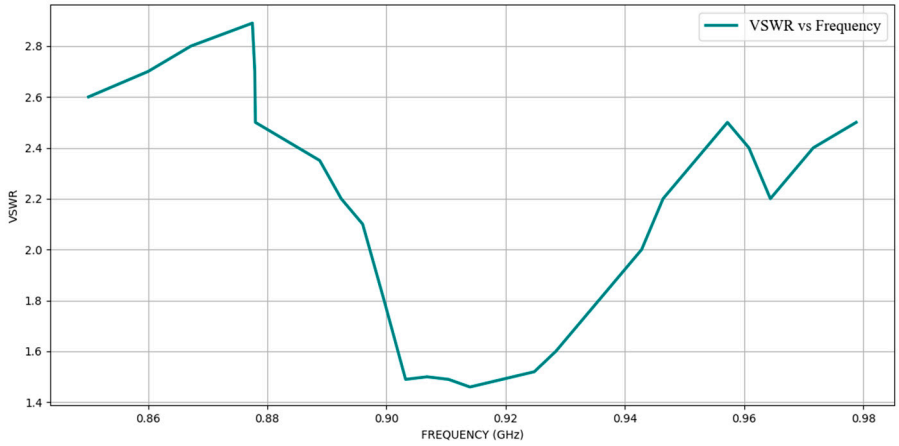

Figure 14. VSWR (unitless) versus frequency (GHz).

5.4. CC-CV Charging of Li-Ion Battery Test

The main objective of this test was to determine whether the designed CC-CV charging algorithm implemented through a step-down DC-DC converter adhered to the correct voltage and current profiles while charging the Li-ion batteries. The following procedure was used to conduct the test: (1) The Li-ion batteries were discharged to 3.0 V per battery, just above their discharge cut-off voltage of 2.75 V, (2) The step-down DC-DC converter was connected to the DC power supply, (3) The voltage probe was connected across the terminals of the Li-ion batteries, (4) The current probe was setup to measure the current flowing through the shunt resistor, (5) The DC power supply was switched on, and (6) The voltage across, and current through the Li-ion batteries was recorded at 2-min intervals. Figure 15 shows the voltage and current profile over a 150 min of the implementing the CC-CV charging algorithm.

The charging system started in constant current mode with a constant current of I_0 = 1.1 A. In constant current mode the voltage across the batteries increased from a starting value of V_0 = 6.0 V. Constant current persisted until the voltage across the batteries reached V_0 = 8.4 V when the charging system switched to constant voltage mode. Once the current started to decrease, the voltage remained constant at V_0 = 8.3 V until the current reached a final value of I_0 = 163 mA. The test was a success. The current remained constant with the voltage across the batteries increasing. Constant current persisted until the voltage across the batteries reached 8.4 V. Thereafter the voltage remained constant with the current decreasing. The test was a success.

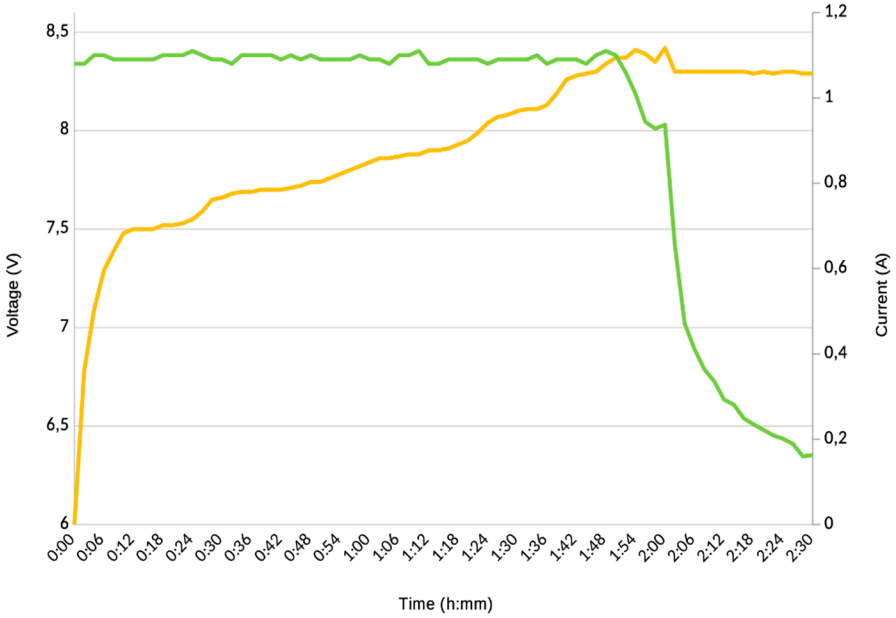

Figure 15. Voltage (V) vs. Time (Minutes).

6. Summary of Results Achieved

This section summarizes all the expectations of the project and the results achieved in Table 6.

Table 6. Summary of expected outcomes and achieved outcomes.

S/N	Intended Outcome	Actual Outcome
1	The power base station should be remote (does not have access to the grid) and derive its power via solar energy.	The power base station was able to derive its power from the solar panel.
2	The power outputted by the solar panel should be conditioned by a DC-DC converter as well as a CCCV (Continuous Current—Continuous Voltage) battery charger to charge the battery correctly.	The batteries were charged correctly through the implementation of a CC-CV charging algorithm controlling the DC-DC converter.
3	The power base station should provide RF energy to the sensor node.	The power base station provided RF energy to the sensor node.
4	The sensor node should be battery-less and wireless.	The sensor node was battery-less and wireless
5	Energy stored by the energy harvesting system should provide power to the sensor node's temperature sensor, microcontroller, and LoRa transceiver.	Energy stored by the energy harvesting system provided power to the sensor node's temperature sensor, microcontroller, and LoRa transceiver.
6	The sensor node should collect data (the sensed temperature) and communicate this data to the user base station using the LoRa LPWAN protocol.	The sensor node collected data and communicated the data to the user base station.
7	The system should measure temperature once every 60 min.	The system measured temperature once every 156 min.
8	The gain of the rectenna should be at least 1 dBi.	The gain of the antenna was 12.62 dBi
9	The voltage applied to the terminals of the battery while charging should not exceed the rated battery charging voltage. For Li-ion (Lithium-ion), this value is 4.2 V.	The voltage applied to the terminals of the battery did not exceed 4.21 V per battery.
10	The current delivered to the battery while charging should not exceed the rated battery charging current. For Li-ion batteries this value is half of the rated battery capacity given in mAh.	The current delivered to the battery while charging did not exceed 1.11 A.
11	The energy harvesting method should provide a minimum voltage of 1.8 V.	The energy harvesting circuit was able to provide 3.3 V.
12	The temperature should be measured once every 60 min.	The temperature was measured once every 156 min
13	The frequency of the RF transmitter should be 920 MHz ± 1.5 kHz. The transmitted RF should be CW (continuous wave) RF.	The frequency of the RF transmitter was 920 MHz ± 1.5 kHz and was a CW.
14	The step-down DC-DC converter, CC-CV charging control system hardware and software, sensor antenna, RF energy harvesting circuit, sensor node energy storage circuitry, sensor node microcontroller firmware should be designed and implemented.	The step-down DC-DC converter, CC-CV charging control system hardware and software, sensor antenna, RF energy harvesting circuit, sensor node energy storage circuitry, sensor node microcontroller firmware were all designed and implemented.

7. Conclusions

In this work, a system that provides a sensor node with energy through RF energy harvesting for a complete off the grid IoT solution has been developed. The hardware and software for the CCCV charging algorithm implemented through the control of the step-down DC-DC converter was designed from first principles. Central to the control of the DC-DC converter was the Microchip PIC32MX220F032

microcontroller. The continuous cycling method was used to determine the ultimate gain and ultimate period of the step-down converter. Tyreus-Luyben PID tuning parameters were used in the DC-DC converter control system. The Yagi antenna was simulated and optimized using FEKO. FEKO was used more proficiently in the design and optimization of the Yagi antenna. The fully cross-coupled RF-DC circuit was simulated using LTSpice XVII. Renesas ultra-high frequency transistors were used in the implementation of the fully cross-coupled RF-DC circuit. A low input voltage step-up DC-DC converter was designed to provide the Multitech MDOT LoRa module and the Microchip MCP9700 temperature sensor with 3.3 V. The firmware residing on the microcontroller contained PD control to ensure that the output is maintained upon the introduction of load. Correct and safe charging of the lithium-ion batteries that power the power base station using solar power and the powering of a sensor node using harvested RF energy over a distance 15 m was achieved. The Yagi antenna achieved a gain of 12.62 dBi and a return loss of −14.11 dB at 920 MH.

Author Contributions: Conceptualization, T.M., A.M.A.-M.; methodology, T.M.; software, T.M.; validation, A.M.A.-M., G.P.H.; formal analysis, T.M.; investigation, T.M.; resources, T.M.; data curation, T.M.; writing—original draft preparation, T.M., S.S.O.; writing—review and editing, S.S.O., A.M.A.-M., G.P.H.; visualization, S.S.O., A.M.A.-M.; supervision, A.M.A.-M., G.P.H.; project administration, A.M.A.-M., G.P.H.; funding acquisition, A.M.A.-M. All authors have read and agreed to the published version of the manuscript.

Funding: This research was supported by the Council for Scientific and Industrial Research, Pretoria, South Africa, through the Smart Networks collaboration initiative and IoT-Factory Programme (Funded by the Department of Science and Innovation (DSI), South Africa).

Conflicts of Interest: The authors declare no conflict of interest. The funders had no role in the design of the study; in the collection, analyses, or interpretation of data; in the writing of the manuscript, or in the decision to publish the results.

References

1. Centenaro, M.; Vangelista, L.; Zanella, A.; Zorzi, M. Long-range communications in unlicensed bands: The rising stars in the IoT and smart city scenarios. *IEEE Wirel. Commun.* **2016**, *23*, 60–67. [CrossRef]
2. Oyewobi, S.; Onwuka, E. Conservation of Mobile Terminals' Battery Life Using Dynamic Power Control Algorithm. *J. Wirel. Network. Commun.* **2012**, *2*, 15–20.
3. Shafique, K.; Khawaja, B.A.; Khurram, M.D.; Sibtain, S.M.; Siddiqui, Y.; Mustaqim, M.; Chattha, H.T.; Yang, X. Energy Harvesting Using a Low-Cost Rectenna for Internet of Things (IoT) Applications. *IEEE Access* **2018**, *6*, 30932–30941. [CrossRef]
4. Oyewobi, S.; Onwuka, E.; Onumanyi, A. Mobile terminals energy: A survey of battery technologies and energy management techniques. *Int. J. Eng. Technol.* **2013**, *3*, 282–286.
5. Minami, M.; Morito, T.; Morikawa, H.; Aoyama, T. Solar biscuit: A battery-less wireless sensor network system for environmental monitoring applications. In Proceedings of the 2nd International Workshop on Networked Sensing Systems, San Diego, CA, USA, 1 June 2005; p. 2007.
6. Bader, S.; Oelmann, B. Enabling battery-less wireless sensor operation using solar energy harvesting at locations with limited solar radiation. In Proceedings of the 2010 Fourth International Conference on Sensor Technologies and Applications, Venice, Italy, 18–25 July 2010; pp. 602–608.
7. Sikder, A.K.; Acar, A.; Aksu, H.; Uluagac, A.S.; Akkaya, K.; Conti, M. IoT-enabled smart lighting systems for smart cities. In Proceedings of the 2018 IEEE 8th Annual Computing and Communication Workshop and Conference (CCWC), Las Vegas, NV, USA, 8–10 January 2018; pp. 639–645.
8. Saffari, A.; Hessar, M.; Naderiparizi, S.; Smith, J.R. Battery-free wireless video streaming camera system. In Proceedings of the 2019 IEEE International Conference on RFID (RFID), Phoenix, AZ, USA, 2–4 April 2019; pp. 1–8.
9. Naderiparizi, S.; Hessar, M.; Talla, V.; Gollakota, S.; Smith, J.R. Towards battery-free {HD} video streaming. In Proceedings of the 15th {USENIX} Symposium on Networked Systems Design and Implementation ({NSDI} 18), Renton, WA, USA, 9–11 April 2018; pp. 233–247.
10. Talla, V.; Kellogg, B.; Gollakota, S.; Smith, J.R. Battery-free cellphone. *Proc. ACM Interact. Mobile Wearable Ubiquitous Technol.* **2017**, *1*, 1–20. [CrossRef]

11. Tresanchez, M.; Pujol, A.; Pallejà, T.; Martínez, D.; Clotet, E.; Palacín, J. An inexpensive wireless smart camera system for IoT applications based on an ARM Cortex-M7 microcontroller. *J. Ubiquitous Syst. Pervasive Netw.* **2019**, *11*, 01–08. [CrossRef]
12. la Rosa, R.; Livreri, P.; Trigona, C.; di Donato, L.; Sorbello, G. Strategies and Techniques for Powering Wireless Sensor Nodes through Energy Harvesting and Wireless Power Transfer. *Sensors* **2019**, *19*, 2660. [CrossRef]
13. Joannopoulos, J.D.; Karalis, A.; Soljacic, M. Wireless Non-Radiative Energy Transfer. U.S. Pantent 9450421B2, 20 September 2016.
14. Oruganti, S.K.; Malik, J.; Lee, J.; Paul, D.; Park, W.; Lee, B.; Seo, S.; Kim, H.S.; Bien, F.; Thundat, T. Experimental and Theoretical Realization of Zenneck Wave-based Non-Radiative, Non-Coupled Wireless Power Transmission. *arXiv* **2019**, arXiv:1903.10294.
15. Wang, J.; Leach, M.; Lim, E.G.; Wang, Z.; Huang, Y. Investigation of magnetic resonance coupling circuit topologies for wireless power transmission. *Microw. Opt. Technol. Lett.* **2019**, *61*, 1755–1763. [CrossRef]
16. Huang, J.; Zhou, Y.; Ning, Z.; Gharavi, H. Wireless Power Transfer and Energy Harvesting: Current Status and Future Prospects. *IEEE Wirel. Commun.* **2019**, *26*, 163–169. [CrossRef] [PubMed]
17. Osepchuk, J.M.; Petersen, R.C. Historical review of RF exposure standards and the International Committee on Electromagnetic Safety (ICES). *Bioelectromagnetics* **2003**, *24*, S7–S16. [CrossRef]
18. Bhattacharya, A.; De, A.; Biswas, A.; Roy, B.; Bhattacharjee, A.K. Application of Particle Swarm Optimization in Design of a Low-Profile Fractal Patch Antenna. In *Advances in Computer, Communication and Control*; Springer: Berlin, Germany, 2019; pp. 207–214.
19. Huang, F.-J.; Yo, T.-C.; Lee, C.-M.; Luo, C.-H. Design of circular polarization antenna with harmonic suppression for rectenna application. *IEEE Antennas Wirel. Propag. Lett.* **2012**, *11*, 592–595. [CrossRef]
20. Clenet, M.; Litzenberger, J.; Lee, D.; Thirakoune, S.; Morin, G.A.; Antar, Y.M. Laminated waveguide as radiating element for array applications. *IEEE Trans. Antennas Propag.* **2006**, *54*, 1481–1487. [CrossRef]
21. Gong, Z.; Wan, K.; Shen, G.; Wan, X.; Wu, R.; Liu, Z.; Lu, Y.; Yin, J. An Ultra-Wideband Capped Bow-Tie Multilayer-Stacked Yagi Antenna. *Prog. Electromagn. Res.* **2019**, *85*, 9–16. [CrossRef]
22. Wahid, P.; Ali, M.; DeLoach, B., Jr. A reconfigurable Yagi antenna for wireless communications. *Microw. Opt. Technol. Lett.* **2003**, *38*, 140–141. [CrossRef]
23. Wu, J.; Zhao, Z.; Nie, Z.; Liu, Q.-H. Bandwidth enhancement of a planar printed quasi-Yagi antenna with size reduction. *IEEE Trans. Antennas Propag.* **2013**, *62*, 463–467. [CrossRef]
24. Galal, H.; Flatae, A.M.; Lagomarsino, S.; Schulte, G.; Wild, C.; Wörner, E.; Gelli, N.; Sciortino, S.; Schönherr, H.; Giuntini, L.; et al. Highly efficient light extraction and directional emission from diamond color centers using planar Yagi-Uda antennas. *arXiv* **2019**, arXiv:1905.03363.
25. Yao, L.; Mao, H.; Batarseh, I.E. A rectification topology for high-current isolated DC-DC converters. *IEEE Trans. Power Electron.* **2007**, *22*, 1522–1530. [CrossRef]
26. Sudevalayam, S.; Kulkarni, P. Energy harvesting sensor nodes: Survey and implications. *IEEE Commun. Surv. Tutor.* **2011**, *13*, 443–461. [CrossRef]
27. Assimonis, S.D.; Daskalakis, S.-N.; Bletsas, A. Sensitive and efficient RF harvesting supply for batteryless backscatter sensor networks. *IEEE Trans. Microw. Theory Tech.* **2016**, *64*, 1327–1338. [CrossRef]
28. Assimonis, S.D.; Fusco, V.; Georgiadis, A.; Samaras, T. Efficient and sensitive electrically small rectenna for ultra-low power RF energy harvesting. *Sci. Rep.* **2018**, *8*, 1–13. [CrossRef] [PubMed]
29. Khullar, V.; Tyagi, H.; Phelan, P.E.; Otanicar, T.P.; Singh, H.; Taylor, R.A. Solar energy harvesting using nanofluids-based concentrating solar collector. *J. Nanotechnol Eng. Med.* **2012**, *3*, 031003. [CrossRef]
30. Pournoori, N.; Khan, M.W.A.; Ukkonen, L.; Björninen, T. RF Energy Harvesting System Integrating a Passive UHF RFID Tag as a Charge Storage Indicator. In Proceedings of the 2018 IEEE International Symposium on Antennas and Propagation & USNC/URSI National Radio Science Meeting, Boston, MA, USA, 8–13 July 2018; pp. 685–686.
31. Ha, B.W.; Park, J.A.; Jin, H.J.; Cho, C.S. Energy transfer and harvesting for RF-Bio applications. In Proceedings of the 2015 IEEE MTT-S 2015 International Microwave Workshop Series on RF and Wireless Technologies for Biomedical and Healthcare Applications (IMWS-BIO), Taipei, Taiwan, 21–23 September 2015; pp. 54–55.
32. Nalini, M.; Kumar, J.N.; Kumar, R.M.; Vignesh, M. Energy harvesting and management from ambient RF radiation. In Proceedings of the 2017 International Conference on Innovations in Green Energy and Healthcare Technologies (IGEHT), Coimbatore, India, 16–18 March 2017; pp. 1–3.

33. Alkheir, A.A.; Mouftah, H.T. Exact statistical characterization of rf-energy harvesting over rice fading channel. In Proceedings of the 2018 IEEE Wireless Power Transfer Conference (WPTC), Montreal, QC, Canada, 3–7 June 2018; pp. 1–4.
34. Lakshmi, P.S.; Jibukumar, M.; Neenu, V. Network lifetime enhancement of multi-hop wireless sensor network by RF energy harvesting. In Proceedings of the 2018 International Conference on Information Networking (ICOIN), Chiang Mai, Thailand, 10–12 January 2018; pp. 738–743.
35. Xu, W.; Kim, J.Y.; Huang, W.; Kanhere, S.; Jha, S.; Hu, W. Measurement, Characterization and Modeling of LoRa Technology in Multi-floor Buildings. *IEEE Internet Things J.* **2019**, *7*, 298–310. [CrossRef]
36. Chevalier, M.; Gomez-Schiavon, M.; Ng, A.H.; El-Samad, H. Design and analysis of a proportional-integral-derivative controller with biological molecules. *Cell Syst.* **2019**, *9*, 338–353.e10. [CrossRef] [PubMed]
37. Liang, Y.; Xu, S.; Hong, K.; Wang, G.; Zeng, T. Neural network modeling and single-neuron proportional–integral–derivative control for hysteresis in piezoelectric actuators. *Meas. Control* **2019**, *52*, 1362–1370. [CrossRef]
38. Eissa, M.A. Novel Fuzzy-Based Self-Adaptive Single Neuron PID Load Frequency Controller for Power System. *Power Electron. Drives* **2019**, *4*, 141–150. [CrossRef]
39. Sun, Y.; Liu, Y.; Tang, N.; Xu, D.; Li, Y.; Yu, Y.; Zhang, K.; Gou, Q.; Du, Z. The design of wideband Quasi-Yagi elliptic dipole antenna with split-ring resonator (SRR) structures. In Proceedings of the 2018 International Workshop on Antenna Technology (iWAT), Nanjing, China, 5–7 March 2018; pp. 1–3.
40. Viezbicke, P.P. *Yagi Antenna Design*; US Government Printing Office: Washington, DC, USA, 1976.
41. Balanis, C.A. *Antenna Theory: Analysis and Design*; John wiley & Sons: Hoboken, NJ, USA, 2016.
42. Zhou, W.; Tong, Z.; Dong, Z.Y.; Wang, Y. LoRa-Hybrid: A LoRaWAN Based Multihop Solution for Regional Microgrid. In Proceedings of the 2019 IEEE 4th International Conference on Computer and Communication Systems (ICCCS), Singapore, 23–25 February 2019; pp. 650–654.
43. Kim, D.-H.; Lee, E.-K.; Kim, J. Experiencing LoRa Network Establishment on a Smart Energy Campus Testbed. *Sustainability* **2019**, *11*, 1917. [CrossRef]